

Development and assessment of a complete ATR algorithm based on ISAR Euler imagery

Baird^{*a}, R. Giles^a, W. E. Nixon^b

^aUniversity of Massachusetts Lowell, Submillimeter-Wave Technology Laboratory (STL)
175 Cabot Street, Lowell, Massachusetts 01854;

^bU.S. Army National Ground Intelligence Center (NGIC)
2055 Boulders Road, Charlottesville, VA 22911

ABSTRACT

The Euler decomposition, when applied to the polarization scattering matrix, attempts to extract phenomenological information about the scattering target. Because the Euler parameters constitute a more physically relevant set of parameters than the traditional HH-VV ISAR representations, they have potential to improve ATR performance. The Euler parameter's usefulness in target recognition, however, is effected by several layers of signature variability. Unfortunately, many of the variability layers are often omitted in a typical ATR study. A complete ATR algorithm was therefore developed that allows for all layers of variability and requires no previous knowledge of the target's position, orientation, or average reflectivity. The complete ATR algorithm was then used to assess the effectiveness of Euler ISAR imagery in target recognition when all layers of variability are considered. The general approach and sub-methods used to construct the complete ATR system will be presented, including the methods to determine the targets orientation, registration, and to compare it to a library of pre-rendered target images. Finally, the performance of the Euler parameters in target recognition using the complete ATR algorithm will be presented.

Keywords: ISAR, Euler, polarimetric, signature, ATR

1. INTRODUCTION

When a polarimetric radar system is used to measure the electromagnetic backscattering of an object at each possible polarization, the complex Radar Cross Section (RCS) values can be formed into the polarization scattering matrix known as the Sinclair matrix [see Eq. (1)].

$$\begin{bmatrix} E_H^r \\ E_V^r \end{bmatrix} = \left(\frac{e^{-ikR}}{2\sqrt{\pi R}} \right) \begin{bmatrix} S_{HH} & S_{HV} \\ S_{VH} & S_{VV} \end{bmatrix} \begin{bmatrix} E_H^t \\ E_V^t \end{bmatrix} \quad (1)$$

In this way, the Sinclair matrix S links the transmitted fields E^t to the received electric fields E^r for the traditional polarizations of Horizontal (H) and Vertical (V). The wave's propagation term in parentheses in Eq. (1) is factored and normalized out.

Use of a polarimetric Inverse Synthetic Aperture Radar (ISAR) system enables the formation of an object's spatial two-dimensional image. The ISAR image contains a spatial map of the object's scattering properties so that the Sinclair matrix is known for each pixel in the image. This image formation is possible because scattering measurements made for a sweep in frequencies as well as for a sweep in azimuthal look angles are spectral assessments of the object's spatial extents. When such a sweep of RCS values for frequency and azimuth are Fourier transformed, the spatial distribution of the object's scattering properties are recovered in a pixelized image.

* Correspondence: Christopher_Baird@student.uml.edu; phone (978) 934-1300; fax (978) 452-3333
SPIE #6547-23

Report Documentation Page				Form Approved OMB No. 0704-0188	
Public reporting burden for the collection of information is estimated to average 1 hour per response, including the time for reviewing instructions, searching existing data sources, gathering and maintaining the data needed, and completing and reviewing the collection of information. Send comments regarding this burden estimate or any other aspect of this collection of information, including suggestions for reducing this burden, to Washington Headquarters Services, Directorate for Information Operations and Reports, 1215 Jefferson Davis Highway, Suite 1204, Arlington VA 22202-4302. Respondents should be aware that notwithstanding any other provision of law, no person shall be subject to a penalty for failing to comply with a collection of information if it does not display a currently valid OMB control number.					
1. REPORT DATE 2007		2. REPORT TYPE		3. DATES COVERED 00-00-2007 to 00-00-2007	
4. TITLE AND SUBTITLE Development and assessment of a complete ATR algorithm based on ISAR Euler imagery				5a. CONTRACT NUMBER	
				5b. GRANT NUMBER	
				5c. PROGRAM ELEMENT NUMBER	
6. AUTHOR(S)				5d. PROJECT NUMBER	
				5e. TASK NUMBER	
				5f. WORK UNIT NUMBER	
7. PERFORMING ORGANIZATION NAME(S) AND ADDRESS(ES) Army National Ground Intelligence Center (NGIC),2055 Boulders Road,Charlottesville,VA,22911				8. PERFORMING ORGANIZATION REPORT NUMBER	
9. SPONSORING/MONITORING AGENCY NAME(S) AND ADDRESS(ES)				10. SPONSOR/MONITOR'S ACRONYM(S)	
				11. SPONSOR/MONITOR'S REPORT NUMBER(S)	
12. DISTRIBUTION/AVAILABILITY STATEMENT Approved for public release; distribution unlimited					
13. SUPPLEMENTARY NOTES					
14. ABSTRACT					
15. SUBJECT TERMS					
16. SECURITY CLASSIFICATION OF:			17. LIMITATION OF ABSTRACT	18. NUMBER OF PAGES 12	19a. NAME OF RESPONSIBLE PERSON
a. REPORT unclassified	b. ABSTRACT unclassified	c. THIS PAGE unclassified			

The Sinclair matrix contains all of the scattering information available about the objects contained in the corresponding pixel, but is in a form that is not particularly intuitive or phenomenological. There exists various decomposition techniques that attempt to transform the Sinclair matrix into parameters that have more phenomenological meaning¹. In particular, the Euler decomposition is one that seeks to diagonalize the Sinclair matrix through a coordinate rotation and then extract the Euler parameters as defined by Kennaugh and Huynen^{2,3}. When applied to the scattering measurements, the Euler decomposition leads to ISAR images of the object's Euler scattering properties.

A conjugate-similarity unitary transform [see Eq. (2)] is the operation required to successfully diagonalize the Sinclair matrix S , as demonstrated first by Autonne⁴. It should be noted that the Sinclair matrix is defined in the Back Scattering Alignment (BSA) coordinate system, in contrast to the Forward Scattering Alignment (FSA) used in optics.

$$S_D = U^T S U \quad (2)$$

As a result of the BSA, the *conjugate* eigenvalue equation must be solved to construct the transform matrix U , instead of the *traditional* eigenvalue equation used in optics. The Euler parameters are then defined in terms of the transform matrix U as shown in Eq. (3) and the diagonalized scattering matrix S_D as shown in Eq. (4).

$$U = \begin{bmatrix} \cos(\tau) & i \sin(\tau) \\ i \sin(\tau) & \cos(\tau) \end{bmatrix} \begin{bmatrix} \cos(\psi) & -\sin(\psi) \\ \sin(\psi) & \cos(\psi) \end{bmatrix} \quad (3)$$

$$S_D = \begin{bmatrix} e^{i\nu} & 0 \\ 0 & e^{-i\nu} \end{bmatrix} \begin{bmatrix} 1 & 0 \\ 0 & \tan(\gamma) \end{bmatrix} m \begin{bmatrix} 1 & 0 \\ 0 & \tan(\gamma) \end{bmatrix} \begin{bmatrix} e^{i\nu} & 0 \\ 0 & e^{-i\nu} \end{bmatrix} \quad (4)$$

These five Euler parameters describe the scattering object's maximum reflectivity m , orientation angle ψ , symmetry τ , bounce angle ν , and polarizability γ . The physical meaning of the Euler parameters can be understood by illustrating the parameters' possible values and some simple shapes representative of these values, as shown in Fig. 1.

To use the Euler parameters, the definitions in Eqs. (3) and (4) must be inverted to yield transform equations establishing the Euler parameters as functions of the measured Sinclair matrix elements. This inversion is best accomplished by switching to a power matrix form known as the Kennaugh matrix that is equivalent to the electric-field scattering matrix. The Kennaugh matrix can then be diagonalized one matrix element at a time through similarity rotations similar to Eq. (2), and the Euler parameters are extracted one by one. The detailed derivation of the Euler transform equations has been presented previously^{5,6}.

Once the Euler transform equations were derived and implemented, the test object Slicy was imaged in a compact radar range as an initial check and intuitive demonstration of the Euler parameters. As found in Fig. 2, Slicy contains a trihedral [see Fig. 2(a)] that shows up properly as having an odd bounce and a dihedral [see Fig. 2(b)] that correctly shows up as even bounce. Slicy also has back corners [see Fig. 2(f)] and a front edge [see Fig. 2(d)] that correctly appear as polarizing. It is interesting to note that Slicy appears almost entirely symmetrical at this resolution. Upon inspection, Slicy can be seen to contain several other notable scattering features that show up in its Euler ISAR images.

Due to their phenomenological nature, the Euler parameters have the potential to improve Automatic Target Recognition (ATR). A complete ATR algorithm was developed that includes all of the layers of target variability encountered in the field and requires no human intervention or previous knowledge of the unknown target. The complete ATR algorithm uses the Euler ISAR images of an unknown object to attempt to match it to an object in the reference library. A persistence optimization method was also developed as part of the complete ATR algorithm that was found to improve performance. The ATR algorithm was tested using ISAR signatures of tanks obtained in previous studies under the support and direction of the U.S. Army's National Ground Intelligence Center (NGIC)^{7,8}.


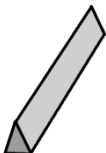

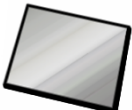












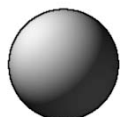
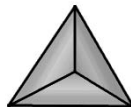

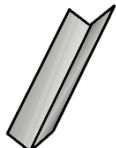
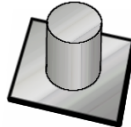

γ	0°	Polarizing			
	45°	Nonpolarizing			
ψ	0°	Horizontal			
	$\pm 90^\circ$	Vertical			
τ	0°	Symmetric			
	$\pm 45^\circ$	Nonsymmetric			
ν	0°	Odd Bounce			
	$\pm 45^\circ$	Even Bounce			

Fig. 1. Sample scattering objects that display the extremes of each Euler parameter.

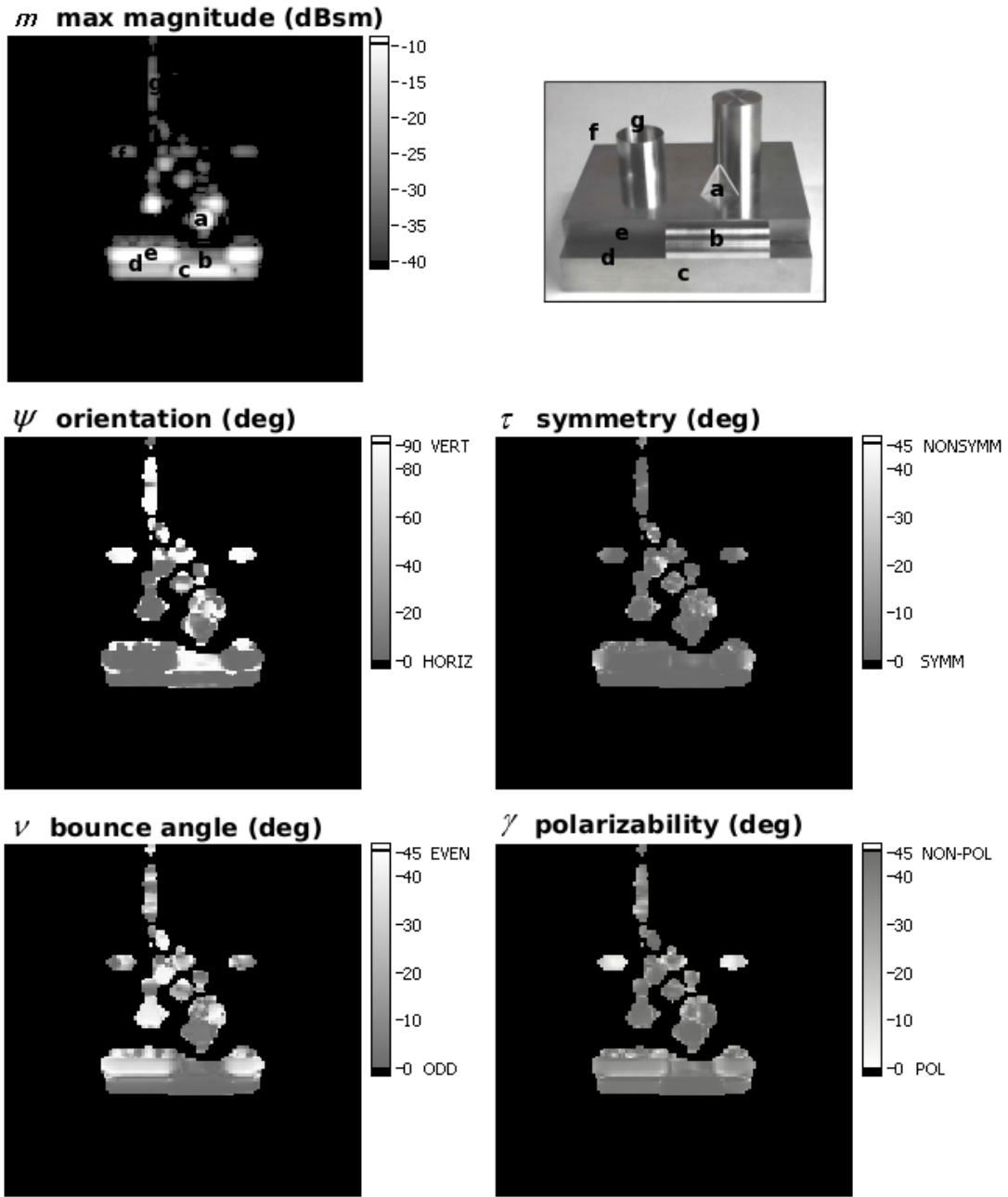


Fig. 2. The test object Slicy and its associated Euler ISAR images measured at 0° azimuth and 5° elevation, demonstrating the physical meaning of each Euler parameter and their applicability to actual measured data.

2. IMPLEMENTATION OF THE ATR ALGORITHM

The ATR algorithm uses enough scattering data to form one polarimetric ISAR image of the unknown object, attempts to match its image to a reference library of previously acquired images, and then assigns the identification of the best matching library object. In order to determine the most effective ATR configuration, the algorithm was designed to

construct and use images in any of the traditional parameter spaces HH, HV, VH, VV, as well as in any of the Euler parameter spaces m , γ , ψ , τ , or v . A persistence optimization was also developed that improves the ATR performance of the Euler parameters.

As outlined in Fig. 3, several steps are involved in the complete ATR algorithm. The library of reference images must be formed before the algorithm can be used. Each object to be included in the library is imaged in a radar range at every possible azimuthal look angle to within 1° and at some fixed elevation angle. Each library image is transformed into Euler ISAR images, thresholded to reduce noise, exactly back-rotated to the common axis of 0° azimuth, and analyzed to determine the persistence-optimization values. The azimuthal persistence of each pixel is calculated as the extent in the azimuthal sequence of ISAR images for which the pixel's values do not change beyond some tolerance band. The more persistent pixels are then assigned greater weights being deemed the more reliable pixels. The persistence weights are stored as part of the reference library and are used during image comparisons to optimize ATR performance.

For the particular library suite of tanks used in this study, a 522 GHz compact range was used with 1/16th scale replicas imaged at a 5.00° elevation angle to match a corresponding 32.625 GHz radar in the field. The scaled tanks were fabricated with scaled material properties through the ERADS partnership and imaged at the University of Massachusetts Lowell Submillimeter Technology Laboratory (STL) under the support of the U.S. Army's National Ground Intelligence Center (NGIC).

When the ATR algorithm is ready to be used, the scattering data of the unknown data is first analyzed to establish its approximate center and azimuthal orientation (see Fig. 3). The object's geometric center is calculated as the center of the distribution of reflected power.

The approximate azimuth of the unknown vehicle is found by assuming a rectangular shape and then finding the angle at which the rotation of the image causes the vehicle's rectangular outline to become parallel to the image's axes. This occurs at the angle at which the one-dimensional profile of the object becomes narrowest, as projected on the image's x-axis. Because the azimuth cannot be determined to a greater accuracy than a few degrees, several possible azimuths are reported and imaged for the one unknown object. When the comparisons are later made for each possible azimuth, the azimuth for which the unknown object's image best matches the library images is retained as the true azimuth.

Once the approximate center and possible azimuths are determined, the scattering data is formed into the ISAR images using Fourier transforms. The image is back-rotated as part of the image formation process by the amount of its azimuth angle in order to align all of the possible images of unknown targets to the common axis at 0° azimuth for proper comparison to the library images which were already back-rotated. Instead of a traditional image rotation, a more exact back-rotation was developed. The traditional image rotation suffers degradation because pixels are assigned to the new non-integer rotated locations but must be rounded to the nearest integer pixel location. The new exact rotation method applies the coordinate rotation *before* the image is formed by the Fourier transforms, and thus avoids the degradation due to rounding. In practice, the novel rotation technique calculates the new non-integer rotated locations and then shifts the Fourier transform to those locations when it is applied as shown in Eq. (5).

$$h(x', y') = \sum_{\phi=0}^{\phi_{\max}} \sum_{f=0}^{f_{\max}} H(\phi, f) e^{-i2\pi f(x \sin \theta + y \cos \theta)} e^{-i2\pi \phi(x \cos \theta - y \sin \theta)} df d\phi \quad (5)$$

Next, the Euler transform equations are applied to each back-rotated ISAR image of the unknown object in order to create Euler ISAR images. The images are thresholded to reduce noise and are ready to be compared to the library images

Each of the unknown object's images formed at the possible azimuths is compared in a brute-force fashion to every possible library object at that azimuth. The comparison of two ISAR images involves registering them through an autocorrelation technique and then computing the Average Percent Difference (APD) between the images. The APD method of establishing a correlation score has been presented and analyzed elsewhere⁹. While the individual pixel

percent differences are being averaged to form the APD, the persistence weights calculated from the azimuthal persistence of the library images are applied to optimize performance. The APD scores of all of the comparisons are tabulated by the algorithm and the comparison with the lowest score is assigned as the unknown object's identification.

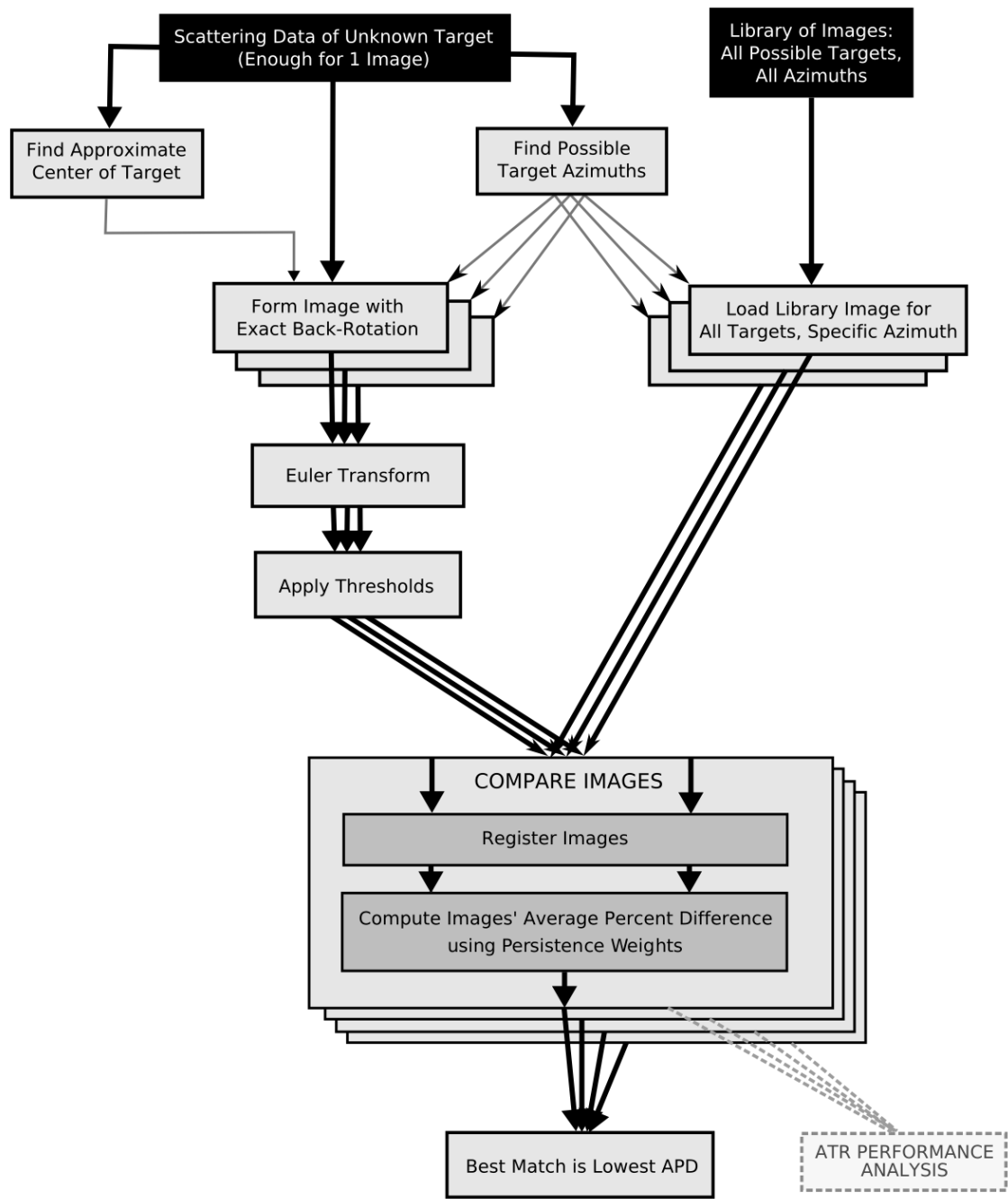


Fig. 3. Schematic process flow of the full ATR algorithm.

3. TESTING THE ATR ALGORITHM

A separate test module was developed which runs hundreds of unknown images from a test suite through the ATR algorithm, compares the identifications to ground truth and establishes performance curves. All of the APD comparisons scores are grouped into histograms and normalized to establish probability density curves. The probability density curves are then scanned as shown in Fig. 4 to construct Receiver Operating Characteristic (ROC) curves. ROC curves are formed by plotting the area of true-positive identifications versus the area of false-positive identification for each possible decision threshold. The closer the ROC curve approaches the top-left corner of the graph, the better the ATR performance. Each ROC curve therefore represents the performance for a specific ATR algorithm configuration when hundreds of tests are done from the test suite.

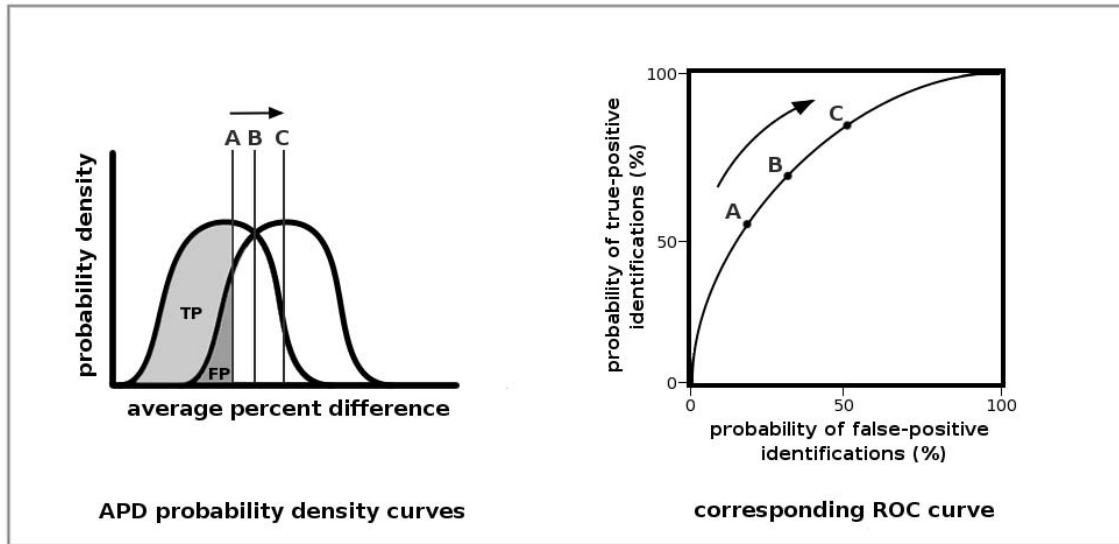


Fig. 4. Schematic diagram of the construction of a ROC from probability curves to analyze ATR performance.

The performance tests were carried out on a suite of similar tanks with differing equipment configurations. It must be stressed that the task of differentiating similar tanks that differ mainly in equipment and not in overall size and shape is among the most difficult tasks that an ATR algorithm can encounter. This challenging test suite was chosen so as to best reveal the effect of the Euler parameters. Two of the tanks from the test suite are presented in Figs. 5 and 6 to illustrate how similar the objects are that must be differentiated by the ATR algorithm. The suite of library images was



Fig. 5. Photo of one of the scaled T-72 M1's used to test the full ATR algorithm.



Fig. 6. Photo of one of the scaled T-72 BK's used to test the full ATR algorithm.

constructed using different measurements of different physical copies of the same tank configurations as in the test suite. Each of the tanks in the test suite and the library suite was measured as 1/16th scaled model replicas in the 522 GHz compact radar range at the University of Massachusetts Lowell Submillimeter Technology Laboratory (STL) to match an equivalent full-scale radar system at 32.625 GHz. The scaled tanks were built through the ERADS program under sponsorship of the United States Army's National Ground Intelligence Center (NGIC) as part of previous studies^{7,8}. Each tank was imaged in free space at a 5.00° elevation angle.

4. ATR PERFORMANCE RESULTS

The ATR algorithm was tested using the entire test suite for different imaging parameters. The results presented in Fig. 7 indicate that the angular Euler parameters ψ , τ , ν , and γ give ROC curves further away from the top-left corner and thus lead to worse target recognition than the traditional imaging parameters HH, HV, VH, and VV. This indicates that although the angular Euler parameters are more phenomenological than the traditional parameters, they are sensitive enough to noise to yield worse performance.

Adjusting the scales on Fig. 7 to zoom in on the top-left corner reveals in Fig. 8 that the Euler parameter m leads to the best ATR performance, better than the traditional parameters.

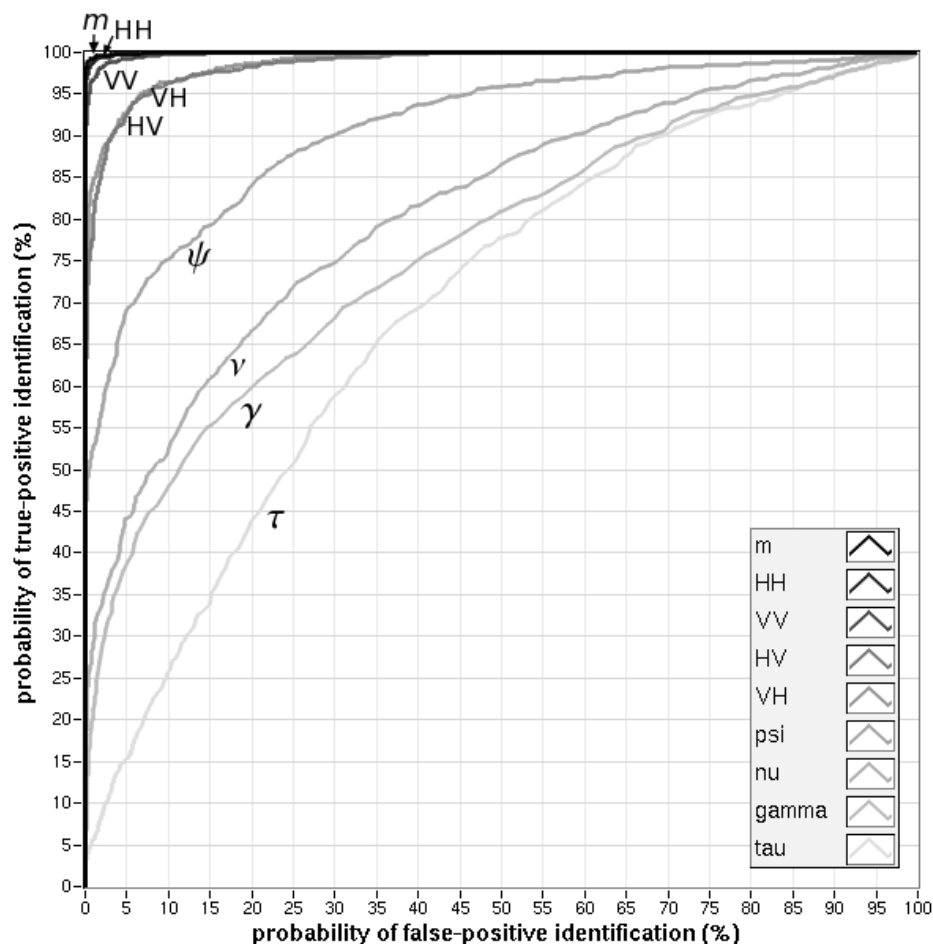


Fig. 7. ROC curves showing ATR performance for the various imaging parameters without persistence optimization.

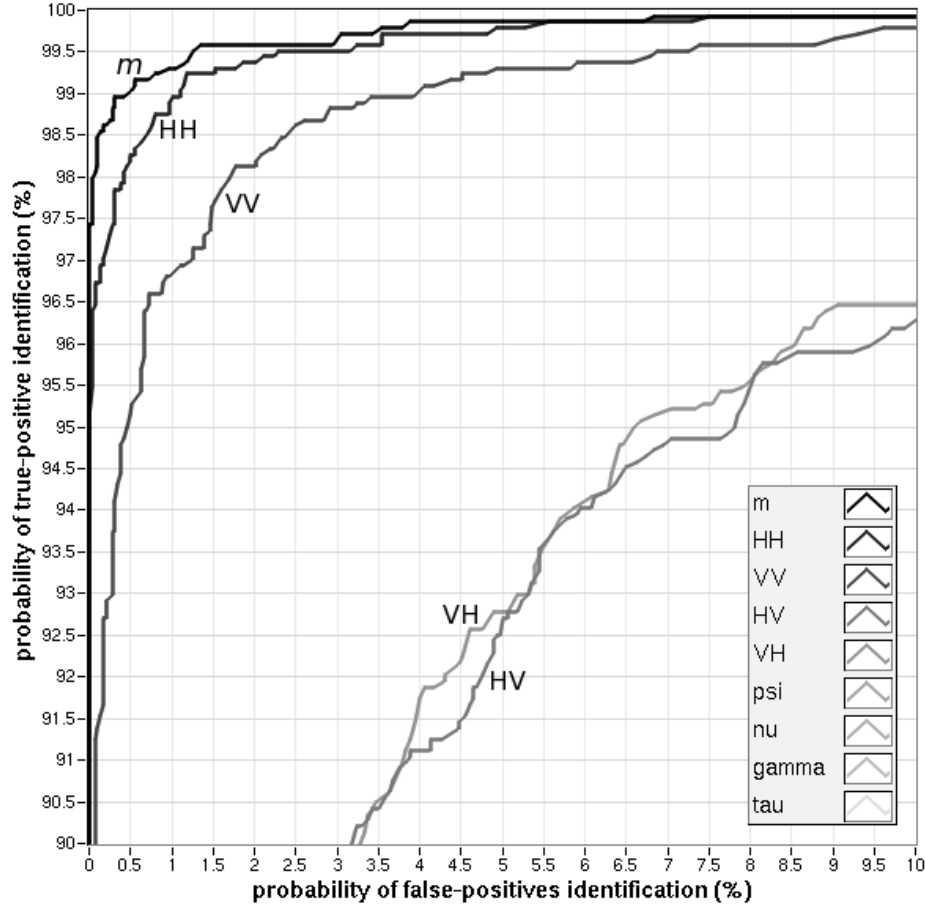


Fig. 8. Zoomed-in ROC curves of ATR performance for the various imaging parameters without persistence optimization.

The results in Figs. 7 and 8 were obtained when no azimuthal persistence optimization was used. When persistence optimization was turned on, the ATR algorithm's performance improved for the angular Euler parameter configurations but did not change much for the magnitude parameter configurations, which includes the Euler parameter m and the traditional parameters HH, HV, VH, VV. Only the ATR performance results for the persistence-optimized Euler polarizability parameter and the traditional parameter HV are shown in Figs. 9 and 10, but they represent all of the angular parameters and magnitude parameter respectively.

The reader must remember that each ROC curve represents the total target recognition performance for a specific ATR algorithm configuration when all of the tanks in the suite are tested at every possible angle, and thus each curve has broader significance than any one individual comparison.

Even with the improvements gained using persistence optimization, the angular Euler parameters still yield worse target recognition than the traditional parameters. It would seem that aside from the Euler parameter m , the Euler parameters are useless in improving target recognition. However, the parameters have only been treated separately up to this point. Because the Euler parameters represent independent scattering properties of the exact same object, they can still improve target recognition when used in a consolidated manner. When implementing consolidation, the scattering data is still imaged into independent Euler images and the different Euler parameter images are still compared to the library images independently, but the independent correlation scores are consolidated to improve performance.

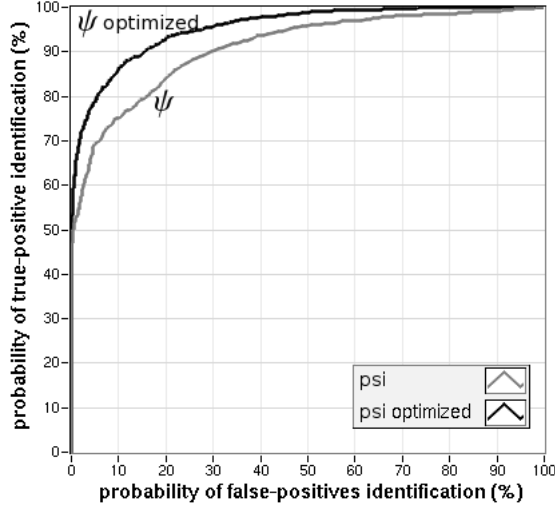


Fig. 9. ROC curves of ATR performance using polarizability images with and without persistence-optimization, representative of all of the angular Euler parameters.

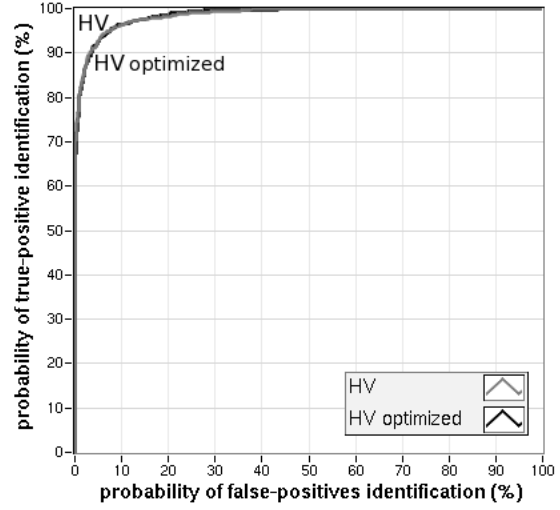


Fig. 10. ROC curves of ATR performance using HV images with and without persistence-optimization, representative of all of the magnitude parameters HH, HV, VH, VV, and m .

The persistence-optimized Euler parameters were combined into a consolidated score s according to Eq. (6). In this equation, s_m , for example, is the correlation score between the unknown vehicle and the library vehicle when they are both imaged in Euler parameter m space. The centering terms s_{m0} , $s_{\gamma0}$, $s_{\tau0}$, $s_{\psi0}$, s_{v0} , in Eq. (6) are fixed constants that are acquired by optimizing them for peak ATR performance using a training set of vehicles separate from the test suite.

$$s = \sqrt{(s_m - s_{m_0})^2 + (s_\gamma - s_{\gamma_0})^2 + (s_\tau - s_{\tau_0})^2 + (s_\psi - s_{\psi_0})^2 + (s_v - s_{v_0})^2} \quad (6)$$

Conceptually, the five independent Euler parameter correlation scores specify a point in five-dimensional space. The consolidated score s defined in Eq. 6 is then the distance in this five-dimensional space from the correlation point to a fixed reference point. The shorter the distance s , the better the two images match.

The final ATR performance results are presented as zoomed-in ROC curves in Fig. 11. The Euler parameter m yields the best target recognition when treated separately, even better than the traditional HH imaging space. However, the best ATR performance was achieved by consolidating the persistence-optimized Euler parameters into a single correlation score s . It should be remembered that these ROC curves represent the target recognition performance of the ATR algorithm for the challenging test suite of spatially similar tanks differing mostly on the level of equipment. Inclusion of spatially different tanks such as the M1 in the test suite were found to only improve the ATR performance results and push the ROC curves further into the top-left corner.

The ROC curve midpoint, shown as a box in Fig. 11, indicates that the ATR algorithm using HH images leads to a 98.9% true-positive identification rate. In contrast, the Euler parameter m gives an ATR performance curve midpoint at 99.4% true-positives. Best of all, the ATR algorithm based on the consolidated Euler score s gives a ROC curve midpoint with a 99.7% true-positive identification rate.

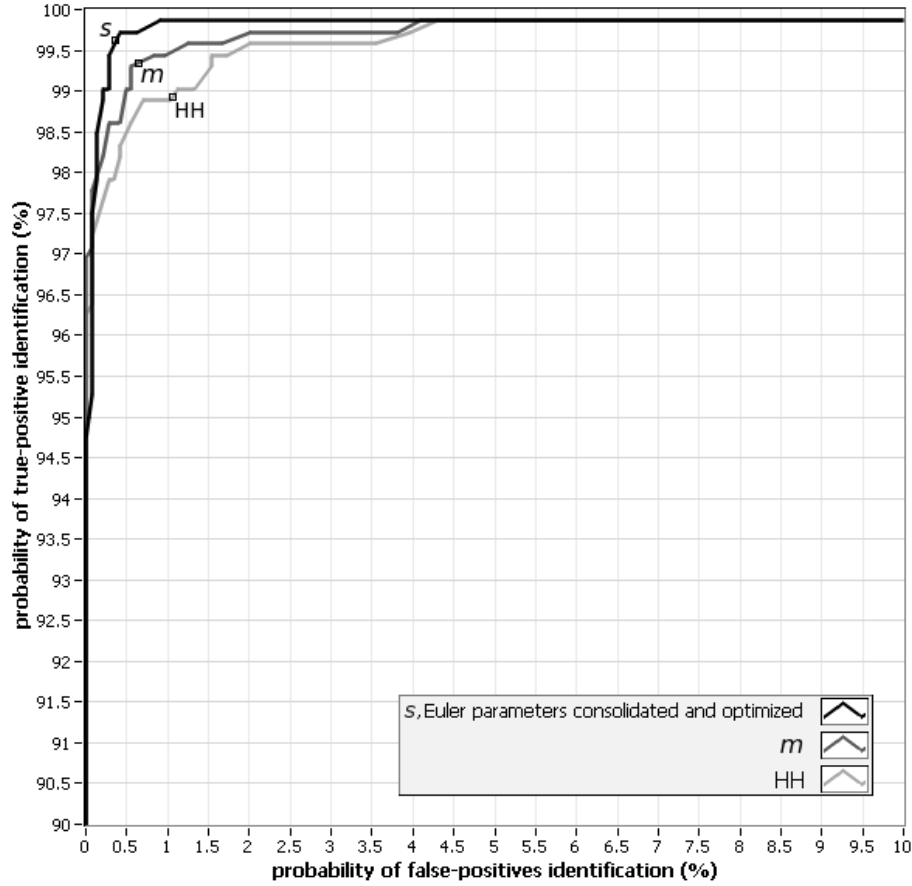


Fig. 11. Zoomed-in ROC curves showing ATR performance for the best three imaging configurations.

5. CONCLUSIONS

A new, full ATR algorithm has been developed using a reference library of high-fidelity radar images, a novel azimuth-identification method, and novel imaging techniques which is shown to successfully recognize targets at high rates. Setting the ATR algorithm to use persistence-optimized Euler parameter images with consolidated correlation scores resulted in better target recognition than the traditional parameter approaches.

REFERENCES

1. C.M.H. Unal, and L.P. Ligthart, "Decomposition Theorems Applied to Random and Stationary Radar Targets," *Prog. In Electromagnetics Research* **18**, 45–66 (1998).
2. E.M. Kennaugh, "Polarization Properties of Radar Reflections," M. Sc. thesis, Ohio State University, Columbus, 1952.
3. J.R. Huynen, "Phenomenological Theory of Radar Targets," Ph. D. thesis, Technical University, Delft, 1970.
4. L. Autonne, "Sur les matrices hypohermitiennes et sur les matrices unitaires," *Annales de l'Universite de Lyon*, **1** (38), 1-77 (1915).

5. C. Baird, W.T. Kersey, R.H. Giles, and W.E. Nixon, "Classification of Targets Using Optimized ISAR Euler Imagery," *SPIE Proceedings*, April 2006
6. J.R. Huynen, "A Revisitation of the Phenomological Approach with Applications to Radar Target Decomposition," Special Report EMID-CL-82-05-18-01, 1982 (unpublished).
7. R.H. Giles, W.T. Kersey, L.C. Perkins, and J. Waldman, "A Variability Study of Ka-Band HRR Polarimetric Signatures on Eleven T-72 Tanks," *SPIE Proceedings*, April 1998.
8. R.H. Giles, W.T. Kersey, M.S. McFarlin, H.J. Neilson, R. Finley, and W.E. Nixon, "A Study of Target Variability and Exact Signature Reproduction Requirements for Ka-Band Radar Data," *SPIE Proceedings*, April 2001.
9. R.H. Giles, W.T. Kersey, and W.E. Nixon, "Correlation of Moving and Stationary Target X-Band Signatures Using ERADS' 160 GHz Compact Range," *48th TriService Symposium*, June 2002.